SAND2021-13273C

20XX-01-XXXX

A Numerical and Experimental Investigation on Different Strategies to Evaluate Heat Release Rate and Performance of a Passive Pre-chamber Ignition System

Author, co-author (Do NOT enter this information. It will be pulled from participant tab in MyTechZone)
Affiliation (Do NOT enter this information. It will be pulled from participant tab in MyTechZone)

Abstract

Pre-chamber ignition has demonstrated capability to increase internal combustion engine in-cylinder burn rates and enable the use of low engine-out pollutant emission combustion strategies. In the present study, newly designed passive pre-chambers with different nozzle-hole patterns – that featured combinations of radial and axial nozzles – were experimentally investigated in an optically accessible, single-cylinder research engine. The pre-chambers analyzed had a narrow throat geometry to increase the velocity of the ejected jets. In addition to a conventional inductive spark igniter, a nanosecond spark ignition system that promotes faster early burn rates was also investigated. Time-resolved visualization of ignition and combustion processes was accomplished through high-speed hydroxyl radical (OH*) chemiluminescence imaging. Pressure was measured during the engine cycle in both the main chamber and pre-chamber to monitor respective combustion progress. Experimental heat release rates (HRR) calculated from the measured pressure profiles were used as inputs for two different GT-Power 1D simulations to evaluate the pre-chamber jet-exit momentum and penetration distance. The first simulation used both the calculated main-chamber and pre-chamber HRR, while the second used only the main chamber HRR with the pre-chamber HRR modeled. Results show discrepancies between the models mainly in the pressurization of the pre-chamber which in turn affected jet penetration rate and highlights the sensitivity of the simulation results to proper input selection. Experimental results further show increased pressurization, with an associated acceleration of jet penetration, when operating with nanosecond spark ignition system regardless of the pre-chamber tip geometry used.

Introduction

To address the threat posed by global warming, countries around the world have continuously strengthened transportation sector efficiency standards to reduce greenhouse gas emissions. In turn, these more stringent efficiency standards have prompted automotive manufacturers to explore alternative engine technologies. One of the most promising technologies to improve efficiency while simultaneously reducing engine-out pollutant emission levels is the lean-burn concept [1]. The increased air-to-fuel ratio for lean-burn combustion results in increased thermodynamic efficiency due to the higher specific heat ratio of the combustible mixture. Compression ratios can also be increased due to decreased prevalence of end-gas auto-ignition [2]. Finally, lower bulk gas temperatures reduce thermal nitrogen oxide (NOx) formation and minimizes cylinder wall, head, and piston surface heat transfer losses. However, these benefits come at the cost of increased cycle-to-cycle combustion variability and the consequent necessity to increase ignition energy. Higher combustion instability may also lead to increased unburned hydrocarbon and carbon monoxide emissions.

In this framework, passive mode pre-chamber ignition is a potential enabler of lean-burn strategies, while maintaining suitable combustion efficiency and stability [3]. One implementation of passive pre-chamber ignition features the use of a small pre-chamber (PC) (around 2-4% of the engine compressed volume) that replaces the conventional spark plug in the main chamber. In this configuration, part of the main charge is scavenged into the PC volume during the compression stroke through nozzles that separate the pre and main chambers. The flammable PC charge is ignited by a spark plug embedded within the pre-chamber housing. The combustion process increases pressure in the PC relative to the main chamber, forcing the ejection of hot combustion jets into the main chamber. Combustion products transferred from the pre-chamber to the main chamber contain active radicals and thermal energy that subsequently ignite the main chamber charge. The PC volume and nozzles geometry can be optimized such that the distribution of hot ejected jets results in an acceleration of the combustion process, which thereby results in sufficient stability and reliability.

Numerous PC ignition experiments have been reported previously with data generated from research engines, vessels, and rapid compression machines (RCMs). Data from these experiments along with companion simulation results from 3D computational fluid dynamics (CFD) simulations have led to improved fundamental knowledge of different flame initiation mechanisms. Attard et al. [4] demonstrated an effective increase in the thermal efficiency and a reduction in the NOx formation with pre-chamber ignition for on-road vehicle engines, even at part loads [5]. Pre-chamber ignition has also been found to benefit efficiency and emissions for stationary power applications [18, 19, 20]. Biswas et al. [6] studied the relationship between the nozzle diameter and pre-chamber volume on combustion performance, while Mastorakos et al. [7] defined separate jet and the flame ignition mechanisms that were dependent whether reactions were quenched at the nozzle exit. Allison et al. [8] focused on the kinetics of premixed combustion and found that the dynamic structure and composition of the turbulent jet controls subsequent ignition processes. Bunce et al. [9] studied the interaction between the pre-chamber and main chamber events, demonstrating that jet velocity is critical to optimize the effectiveness of turbulent jet ignition in the main chamber. Muller et al. [10] used 3D CFD to study the ignition mechanism of lean mixtures by hot turbulent jets and found that the flow dynamics strongly influence the mixing process near the flame front. Combustion visualization within an optically accessible single-cylinder research engine (SCRE) carried out by Gentz et al. [11] demonstrated that the auxiliary fuel injection was critical for combustion stability. The RCM experiments carried out by Gholamisheeri et al. [12] showed that several theoretical correlations are in good agreement with the experimental observations. Many CFD simulations were performed by Jamrozik et al. [13], Thelen et al. [14], Wang et al. [15] and Novella et al. [16, 17], which focused on the key aspects of the pre-chamber ignition concept that are not easily interrogated experimentally, which includes internal mixing and heat transfer processes within the pre-chamber volume.

A central challenge for CFD of PC ignition is that cycle-to-cycle dispersion may result in simulation divergence. Numerical results are highly dependent on the inputs selection with significant divergence possible when using experimentally obtained inputs such as the combustion progress or from numerical approximations. Garcia-Oliver et al. [21] developed a procedure to select an adequate cycle without divergence that was adopted for the present study.

The numerical and experimental studies cited above have shown that the evaluation of different pre-chamber ignition concepts and the associated effects on heat release and jet performance are still poorly understood. Pressurization of the pre-chamber has been observed to be a critical aspect to obtain suitable reactive jets [22], so introducing different ignition systems to achieve a faster and stronger combustion process inside the pre-chamber could improve performance as in-cylinder excess air rates are increased. The present study consists of 2 parts. First, 1D numerical tools were used to evaluate jet momentum flux and penetration distance that made use of input experimental PC and main-chamber pressure-rise data as a boundary condition. Second, the use of a high-energy nanosecond spark igniter that results in faster early flame development was evaluated. Analysis methods follow those outlined previously by the authors [21, 22, 23, 24].

Experimental and Numerical Setup

Sandia Single-Cylinder Optical Engine and Test Bench

Experimental activities were carried out in a 4-stroke, optically-accessible SCRE developed by General Motors (SG2). Engine characteristics were described in detail in previous studies [25, 26], so only important features will be discussed here. A schematic of the engine and test bench is presented in Figure 1 (a). The engine featured a geometrical compression ratio of 13:1. An injector (Bosch HDEV 1.2) with 8 uniformly spaced nozzles with a diameter of 125 µm and a 60° spray angle was used to centrally deliver fuel into the main combustion chamber. A homogeneous fuel/air mixture was generated by a single fuel injection at 300^{o} crank angles (^{o}CA) before top dead center (TDC). Mild charge heating was produced from modest retention of residual burned gases by a relatively short positive valve overlap of 34 ^{o}CA centered at TDC. A motoring dynamometer was used to keep the engine speed constant at 1300 rpm. An optical encoder with a resolution of 0.1 ^{o}CA was implemented to measure crank location. The temperature of the cylinder wall and engine head was maintained constant at 90 ^{o}C, via a water-based Aquatherm heat exchanger. In Table 1, the main specifications and characteristics of the engine can be found. In this study, RD58-7 research grade gasoline was utilized, and its key properties are reported in Table 2.

The intake air supply was precisely controlled via a Tescom ER5000 PID (Proportional, Integral, Derivative) pneumatic flow controller. Resistive heaters were utilized to heat the intake and exhaust runners. The intake air supply was heated to 62 °C by a Chromalox circulation heater located upstream of the intake plenum. Pollutant emissions were monitored by means of three different emissions analyzers connected to the exhaust plenum via heated exhaust lines. Carbon monoxide (CO), carbon dioxide (CO2), and oxygen (O2) were monitored with a CAI 600 NDIR/Oxygen Multi-Component analyzer. A CAI 600 HFID analyzer was used to measure unburned hydrocarbon (HC). Finally, Nox emissions were measure by a CAI 600 HCLD NO/Nox. The in-cylinder pressure was measured by piezo-electric pressure sensor (Kistler 6135A).

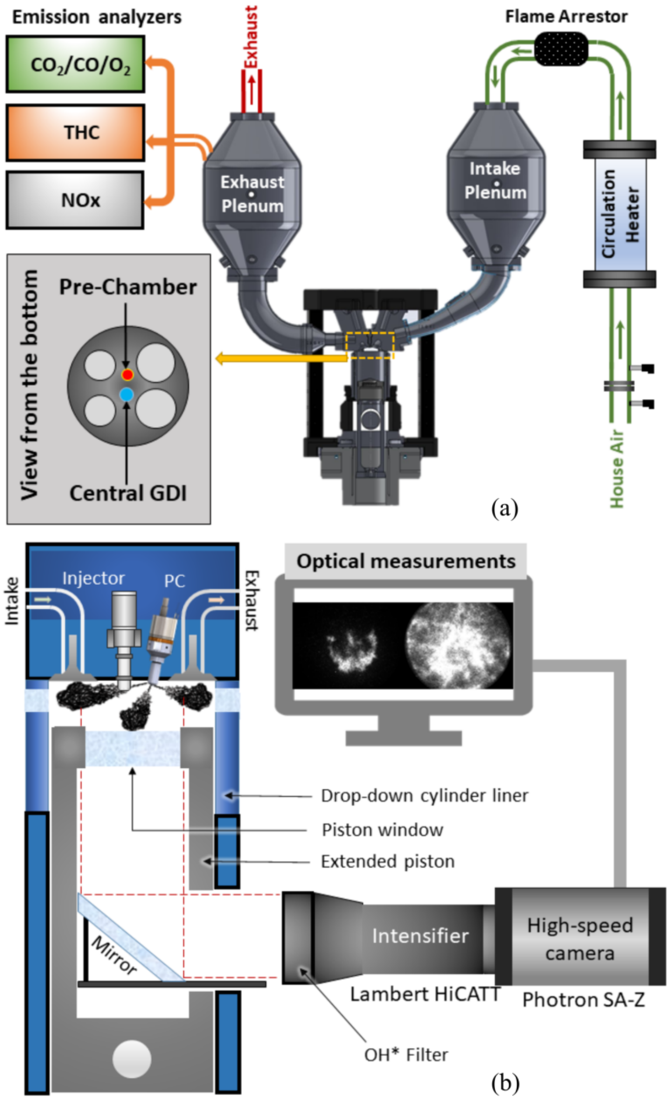

Figure 1. Schematic of the engine and test bench (a), and high-speed OH* chemiluminescence imaging via a Bowditch-type optical piston (b).

To visualize main-chamber ignition and combustion, images of hydroxyl radical (OH*) chemiluminescence were collected from below via a Bowditch pistion, through a window mounted in the base of the piston bowl, as shown in Figure 1 (b). A high-speed camera (Photron SA-Z) connected to a Lambert high-speed HiCATT intensifier and 105 mm UV f/2.8 Nikkor lens was utilized to collect the chemiluminescence emissions from the combustion process. The camera was operated at 40,000 frames per second (0.2 °CA resolution at 1300 rpm), with a field of view of 896×448-pixel, to resolve the dynamics of the jets of hot gases exiting the pre-chamber. A gate of 12 µs and a gain of 850 was set for the intensifier. A 5 nm narrowband filter centered at 420 nm was utilized to isolate OH* emission as a marker of the flame front.

Table 1. Main specifications and characteristic of the engine.

Displaced volume w/o PC [cm3]	551
Bore/Stroke/Connecting Rod [mm]	86/95.1/ 166.7
Geometric Compression Ratio w/o PC	13:1
Number of Valves	4
Intake Valve Open/Close [°TDC]	343 / -145
Exhaust Valve Open/Close [°TDC]	160 / -343
Maximum Valve Lift [mm]	9.7
Fuel Injection Pressure [bar]	100
Injection system	DI
Injector Hole Number	8
Injector Cone Angle [°]	60
Injector Orifice Diameter [µm]	125
Intake Pressure [kPa]	51 – 61
Exhaust Pressure [kPa]	104
Intake Temperature [°C]	62
Engine Speed [rpm]	1300
Cycle fueling rates [mg/cycle]	14.3 – 14.9
Equivalence ratio	0.7 – 1.00
Spark Timing [°TDC]	-24 – -5

Table 2. Properties of the fuel (RD58-7)

Liquid Density @15 °C [g/L]	748
LHV [MJ/kg]	41.9
H/C ratio	1.972
O/C ratio	0.033
Research Octane Number	92.1
Octane Sensitivity	7.3
T10 / T50 / T90 [°C]	57 / 98 / 156

Two different ignition systems were used to ignite the mixture inside the pre-chambers. The first was a conventional inductive spark plug (ISP) ignition system used baseline the pre-chamber performance. A 12 V power supply was connected and charging an ignition coil for 4 ms. The coil was connected to a spark plug (NGK ER9EHIX) with a 0.7 mm electrode gap. The second ignition system was designed to generate nanosecond repetitive pulsed (NRP) plasma discharges, with a duration of 12 ns full-width at half maximum. In this system, a nanosecond DC pulse generator (Transient Plasma Systems Inc.) was connected to a spark plug (NGK 7473) with a 0.9 mm electrodes gap.

Passive pre-chamber geometry and diagnostics

Pre-chamber geometries were designed following an in-house methodology developed at CMT-Motores Termicos that combines a 1D wave action model and a 1D jet model [24]. Schematics of the pre-chambers utilized in this work are presented in Figure 2. The pre-chamber assembly is divided into a tip and body (Figure 2 (a)) to facilitate rapid exchange of tips and ignition systems. The pre-chamber body housed the spark plug and a piezo-electric pressure transducer (AVL GH14P) used to monitor the pressure inside the pre-chamber volume. Two tips were investigated, PC 1 and PC 2, and their main geometrical parameters are reported in Table 3. Both tips were tested with the two ignition systems. Both pre-chamber tips have a narrow throat geometry that increases the jet ejection velocity due to the throttling effect of the nozzles, which benefits the main chamber sweep and ignition. The tips have different internal volumes that corresponded to 4.76% and 4% of the compressed volume of the engine for PC 1 and PC 2 respectively. Both tips have 6 radial nozzles. However, PC 1 has smaller nozzle diameters than PC 2, to compensate for the additional axial nozzle that this tip features to improve the scavenging and filling of the pre-chamber. A modest 12.5° tangential angle was adopted to improve mixing fresh scavenged charge and retained pre-chamber combustion residuals from the previous cycle to promote more repeatable combustion inside the pre-chamber [24].

Table 3. Main geometrical specifications of the pre-chambers.

Tip	PC 1	PC 2
Volume [cm3]	2.0	1.7
Radial nozzle	6	6
Radial nozzles diameter [mm]	0.8	1.2
Axial nozzle	1	0
Axial nozzle diameter [mm]	1.0	-
Total nozzle area [mm^2]	3.8	6.8
Nozzles tangential angle [°]	12.5	12.5

Numerical models description

As stated in the introduction, the main goal of this work is to evaluate the differences between two models utilized within the framework of a commercial 1D wave action software, GT-Power, when using either numerically imposed or experimentally obtained heat release rates (HRR) as inputs. Following this evaluation, a 1D jet model was utilized to estimate the pre-chamber jet penetration and velocity, and highlight the sensitivity of the simulations to the input selection.

1D Wave action model

The models in the 1D wave action software included several sub-models that evaluate not only the performance of the pre- and main chambers, but also several relevant parameters, such as jet momentum flux, temperature and fuel mass inside the pre-chamber. These models were focused only on the closed part of the engine cycle from intake valve closure (IVC) to exhaust valve opening (EVO) where ignition, combustion and ejection processes occur [21].

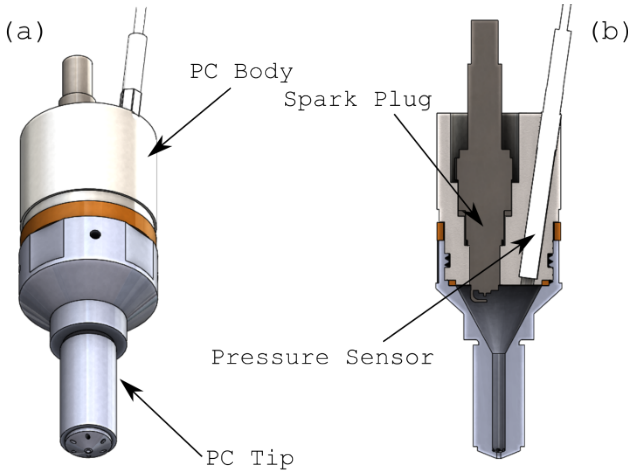

Figure 2. Schematic of the pre-chambers. The schematic shows the PC 1 including radial and axial nozzles. The PC 2 has a similar geometry but does not have the axial nozzle.

In the 1D wave action code, the two chambers were connected by a series of channels that approximate the pre-chamber nozzles. Since the pre-chamber was modeled as a non-moving piston, the code was able to simulate the evolution of pressure in both chambers as well as the mass and energy exchange between them using heat release profiles. These heat release profiles could be imposed from the experiments or simulated by means of a normalized Wiebe function. The mass flow rate and the gas velocity were recorded in one of the radial nozzles to estimate the resulting jet momentum flux, which was utilized as input for the 1D jet model. The evolution of the gases in both chambers was simulated as a perfectly-mixed homogeneous mixture that evolves as the combustion process advances. In this way, ejected jets in the 1D tool were a mixture of unburned gases (air and fuel) and products of the combustion process (CO, CO_2, H_2O, N_2). The calibration of the model was performed by setting pressure and temperature at IVC and varying heat release settings, heat transfer and discharge coefficients until the simulated pressure profile of main and pre-chamber were similar to those obtained experimentally. Experimental (blue) and simulated (orange) pressure profiles for each chamber are plotted in Figure 3, for the engine operated using PC 1 at the stoichiometric condition. Here it can also be observed that the model is able to well reproduce both the main and pre-chamber pressure trends. Main combustion-related parameters such as indicated mean effective pressure (IMEP) and the 50% burn angle (CA50) presented in Table 4 were also well-matched between the experiment and simulation.

Table 4. Main parameters of the validation process.

	Experimental	Simulated
Max. pressure	27.85 bar	28.87 bar
Injected fuel mass	15.05 mg	14.95 mg
IMEPg	3.54 bar	3.8 bar
CA50	11.2 cad	10.7 cad
ϕ	1	1.01

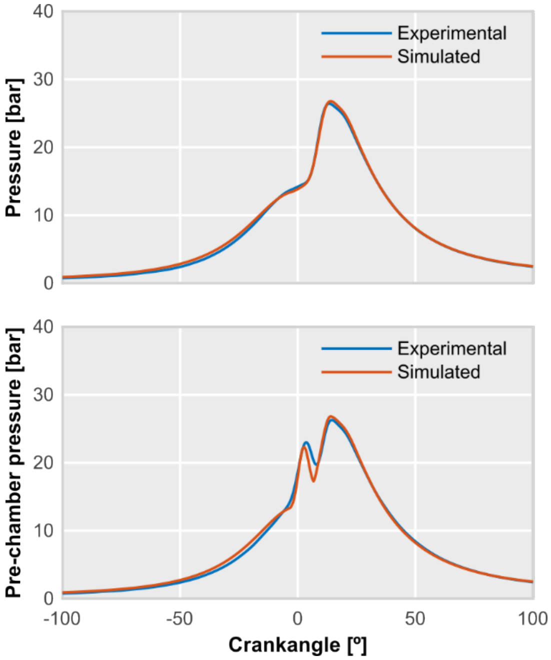

Figure 3. In-cylinder and pre-chamber pressure profiles for experimental and simulated cycles for pre-chamber 1 operating with ISP concept at stoichiometric conditions. The blue line corresponds to experimental profiles and the orange line corresponds to simulated profiles.

1D Jet model

The 1D jet model utilized in this work was similar to the one used previously [21]. As discussed in the other article, the 1D jet model was adapted from an existing model whose main applications involved diesel-like sprays [27, 28, 29]. The current model was modified to simulate gaseous jets from a pre-chamber configuration. The assumptions for a proper gaseous jet simulation were similar to previous ones presented by the authors in [21], so only the main hypotheses are listed here:

- Turbulent mixing of hot ejected pre-chamber gases with the mixture in the main chamber was considered.
- Only free-jet propagation was accounted for, while the interaction between piston-bowl surface and jets was omitted.
- Inputs of the 1D jet model were the temporal evolution of mass flow and the jet momentum flux through one pre-chamber nozzle. Inputs were obtained from the 1D wave action model.
- Main chamber pressure and density were obtained from the 1D wave action model.
- The pre-chamber gaseous jets were modeled as a gas stream that passed through the pre-chamber nozzles and into the main chamber, which was filled with a perfectly mixed air and fuel mixture. The ideal gas equation of state and a low Mach approach were both assumed.
- The gaseous jets were assumed to be a stream of high temperature fluid (around 1500K) that were ejected into a lower temperature chamber (700K). The temperature and mixture composition at the exit of one of the pre-chamber nozzles were assumed to be time independent, to simplify the calculations.
- The radial cone angle was set at 25º for all cases to accommodate for the initial part of the ejection process. This initial part can be difficult to simulate in this kind of 1D

models due to the uncertainties of the very first time step of flow ejection.

Experimental and Numerical Procedure

Experimental procedure

The experimental data presented and discussed in this manuscript were collected with the following procedure. First, the intake air flow rate was set to the desired value and the engine was motored for at least 1000 cycles to warm up the pre-chamber and main chamber surfaces. Then, the engine was fired until combustion and pollutant emissions were stable (CoV < 5%). The fuel flow rate and spark timing (ST) were adjusted to maintain a gross IMEP of 3.5 bar. Therefore, the main parameters, such as in-cylinder and PC pressure, air and fuel flow rate, and emissions were collected for 100 cycles. In 10 of these 100 cycles, 200 images of OH* chemiluminescence were captured at each cycle. At the end of each test, the engine liner was dropped to clean and oil the piston rings, and the entire procedure was repeated. The equivalence ratio of the charge was decreased from 1 to the lean limit, which depended on the PC tip, with a step of 0.1, which was obtained by increasing the flow rate of intake air with a step of 0.1 g/s, while the fuel flow rate was adjusted to maintain a constant 3.5 bar IMEPg. The lean limit was defined when the CoV of this specific condition was greater than 5% or numerous misfire events were observed.

Different experimental procedures were followed for the two ignition systems. For the ISP ignition system, the coil charging time was set to a constant value of 4 ms. However, the control variables of the NRP ignition system were adjusted during the firing of the engine. Specifically, the applied voltage and the number of pulses were minimized to obtain a stable combustion process. The applied voltage was varied from 19 to 26 kV, while either 2 or 5 pulses were used depending on the operating condition.

The apparent heat release in the main combustion chamber was estimated based on the measurement of in-cylinder pressure. A two-zones model was employed so the combustion chamber was divided into two separate zones, one filled with burned gases and one filled with unburned gases, assuming complete combustion in the burned regime. The modified Woschni correlation optimized for lean gasoline compression combustion [30] was utilized to estimate heat losses from the combustion chamber.

The OH* chemiluminescence images were post-processed to estimate the initial velocity of the hot jets exiting the pre-chambers. It is important to note that this analysis was performed only for PC 2, since the presence of the axial nozzle and the imaging angle made impossible to estimate the jet velocity for tip PC 1. First, the images were corrected for background noise (see Figure 4 (a)), and then binarized (see Figure 4 (c)). Therefore, each of the six radial jets was isolated (see Figure 4 (b)) and the furthermost point of the jet boundary from the injection point was identified (see Figure 4 (c)). The initial jet velocity was estimated by tracking this point for 0.1 ms after the start of the ejection. The value of the initial jet velocity was evaluated as an average from all the six jets and the ten imaging cycles at each operating condition. It was not possible to track the furthermost point after 0.1 ms, since part of the main chamber charge was igniting, making the pre-chamber jet boundary indistinguishable.

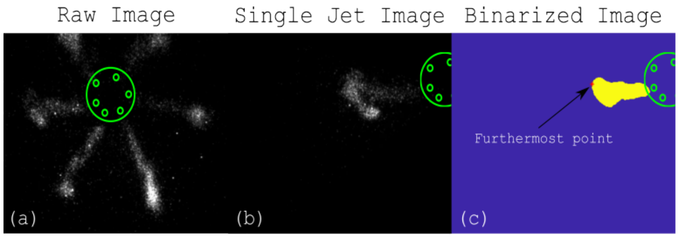

Figure 4: Post-processing of the OH* chemiluminescence images. The raw image (a), the image of a single jet (b), and binarized image (c) of the jet are presented. The schematic of the pre-chamber nozzles pattern is reported in green.

Experimental pre-chamber heat release calculation

The evaluation of the experimental heat release in the pre-chamber was performed utilizing the model developed by Duong et al. [31], also utilized in [32, 33]. Pre-chamber heat release is obtained from Equations 1 and 2 as follows:

$$\frac{dQ_{PC}}{d\theta} = \frac{1}{\gamma - 1} V_{PC} \frac{dP_{PC}}{d\theta} - C_P T_{PC} \frac{dm}{d\theta} \tag{1}$$

Specific heat ratio (γ) and specific heat capacity at constant pressure (C_p) were obtained from the gas temperature of the charge and the mixture fraction of trapped mass in the main chamber. The difference in crank angle degrees is represented as dθ. Equation 2 describes the mass exchange between chambers:

$$dm = \frac{C_d A_T P_{PC}}{\sqrt{R T_{PC}}} \left(\frac{P_{MC}}{P_{PC}}\right)^{\frac{1}{\gamma}} \left(\frac{2\gamma}{\gamma - 1}\left(1 - \left(\frac{P_{MC}}{P_{PC}}\right)^{\frac{\gamma-1}{\gamma}}\right)\right)^{\frac{1}{\gamma}} \tag{2}$$

The adopted convention is that the mass transfer rate (dm) is positive when the pressure in the pre-chamber is higher than in the main chamber. When the pressure in the main chamber is greater than in the pre-chamber, the pressure ratio (P_{mc}/P_{pc}) has to be inverted. Moreover, the temperature and pressure in the first term of Equation 2 has to be changed to the temperature and pressure of the main chamber. The discharge coefficient (C_d) is obtained from the 1D wave action model, while A_t is the total area of the pre-chamber nozzles.

Numerical procedure

The numerical data presented and discussed in this work were evaluated using three different methods:

- The first method was a prediction of an AHRR profile compatible with passive pre-chamber applications prior to obtaining experimental results. The AHRR was modeled as a Wiebe function with combustion phasing (CA50) and combustion duration as modeling parameters. The selected pressure and temperature at IVC, main chamber heat release rate and spark timing were compatible with the experimental results. This method was used for obtaining the predicted

AHRR profile, referred as "Simulation (predicted)" in the following section.

- The second method involved mode calibration with experimentally measured pressure and temperature at IVC, main chamber heat release rate, spark timing and the main geometrical parameters of the pre-chamber. Pre-chamber heat release was then modeled as a Wiebe function with combustion phasing (CA50) and combustion duration modified until the simulated pressure in the pre-chamber matched the pressure measured experimentally. This method was used for obtaining the matched to the experiment AHRR profile, referred as "Simulation (match exp.)" in the following sections.
- The third method was identical to the second except that measured pre-chamber heat release rates were directly implemented into the 1D wave action model instead of modeled as described above. The results obtained with this method are referred as "Simulation (exp. data)" in the following sections.

The selection of the most suitable cycle for the numerical analysis was done following the same methodology as in previous work [21], since it was observed that the average cycle can perform poorly at conditions where cycle-to-cycle variability is significant. A similar merit function was used to identify the most suitable cycle that made use of the maximum pressure and corresponding crank angle of occurrence as well as the start and end of combustion. These metrics are especially relevant at equivalence ratios well below stoichiometric where dispersion may affect the calculation of the average cycle.

Numerical simulations are reported at three equivalence ratios: stoichiometric ($\phi = 1.00$), medium lean case ($\phi = 0.85$) and leanest case ($\phi = 0.75$) for each ignition systems. These operating points were selected to highlight the main differences in terms of jet performance, with decreasing equivalence ratio.

The main results of the 1D wave action model were used as inputs for the 1D jet model, and included jet momentum flux profiles as well as mass flow rates for a single PC radial nozzles, and main chamber pressure and density. Consequently, the temporal evolution of the jet penetration was calculated, which allowed an estimation of the jet velocity and the time needed for reaching cylinder walls.

Results and Discussion

Evolution of the experimental apparent heat release rate and pressure in the pre-chamber

Apparent heat release rate (AHRR) profiles are plotted for PC 1 and PC 2 in Figure 5 (a) and 5 (b) respectively, for both the NRP and ISP ignition systems. The calculation of these profiles was performed using experimentally measured pressures and Equations 1 and 2.

It is immediately notable that the NRP igniter uniformly produced the expected increased HRR relative to the ISP igniter for both PC 1 and PC 2 at each corresponding equivalence ratio. The increased PC HRR for NRP likely is due to increased ignition energy deposition that in-turn accelerates early kernel expansion as compared to the ISP system. The biggest increase was for PC 1, which had peak HRR values increase by between 30 and 50% with NRP with a more modest 10 – 20% HRR increase for PC 2. The reduced effectiveness of NRP for PC 2 may be due to the smaller 1.7 cm^3 internal volume relative to the larger 2.0 cm^3 internal volume for PC 1, which makes PC 2 more susceptible to earlier flame wall quench. It may also be due to better scavenging for PC 1 due to the presence of an axial nozzle.

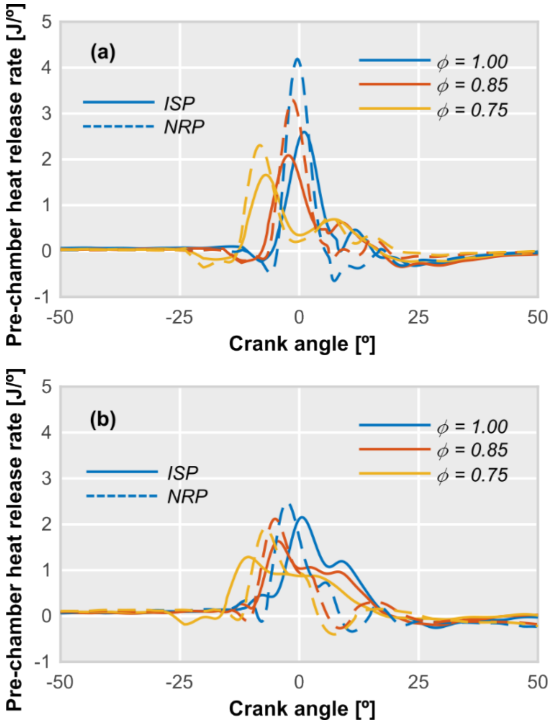

Figure 5. Apparent heat release rate profiles for the three operating points of PC 1 (a) and PC 2 (b) and both ignition systems. The solid line corresponds to the ISP system, dashed line corresponds to the NRP system. The blue, orange and yellow line correspond to $\phi = 1.00$, $\phi = 0.85$ and $\phi = 0.75$, respectively.

Peak pre-chamber HRR as well as the initial HRR slope both decreased with a decrease in main-chamber equivalence ratio for both PC tips and igniters investigated, which has been attributed to slower flame propagation with leaner mixtures. The reduction in flame speeds was exacerbated by retained residuals within the pre-chamber that added additional dilution to fuel and air scavenged from the main chamber.

The evolution of the experimentally measured pressure difference (ΔP) between the main and pre-chamber is plotted in Figure 6 (a) and 6 (b) for PC 1 and PC 2, respectively. For each pre-chamber geometry, there was clear correlation between HRR profiles and ΔP, with the NRP igniter producing the largest difference for a given PC geometry and stoichiometry that was proportional to the increase in HRR. For the respective pre-chamber geometries, PC 2 had a roughly factor of 4 decrease in ΔP relative to PC 1 for the same igniter-equivalence ratio combination. Two factors are likely in play here. First, the smaller PC volume for PC 2 resulted in lower total heat release. Second, the combined nozzle hole area for PC 2 is around 79% larger than for PC 1 (see Table 3), which consequently provided less restriction for mass transfer out of the pre-chamber and hence a reduction in PC pressure build-up.

Numerical evaluation of pre-chamber performance

After obtaining pre-chamber AHRR measurements, these data were used to numerically evaluate the pre-chamber jet momentum flux and penetration distance using the 1D wave action model described previously. The jet momentum flux profile for a single radial nozzle is plotted in Figure 7 (a) for PC 1 and Figure 7 (b) for PC 2.

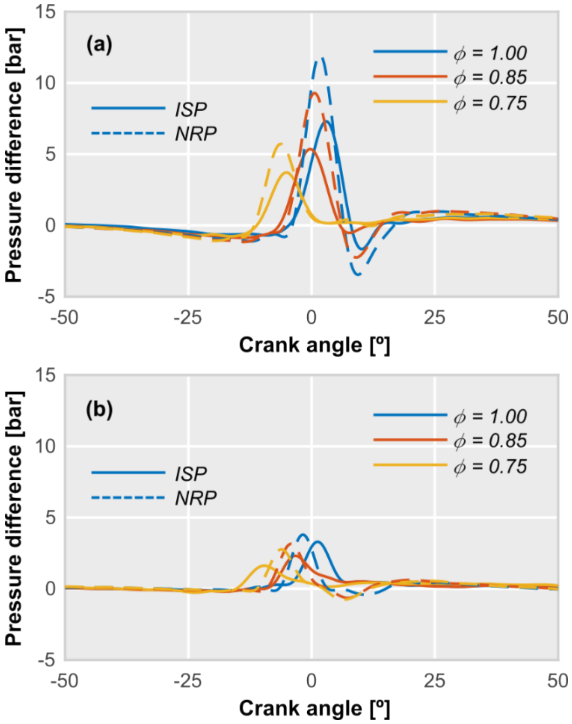

Figure 6. Evolution of the pressure difference between chambers for the three operating points of PC 1 (a) and PC 2 (b) and both ignition systems. The solid line corresponds to the ISP system, the dashed line corresponds to the NRP system. The blue, orange and yellow lines correspond to ϕ = 1.00, ϕ = 0.85 and ϕ = 0.75, respectively.

For each PC geometry, jet momentum flux was directly proportional to ΔP. Accordingly, the use of NRP igniters led to increased jet momentum flux as compared to the use of ISP igniters for any pre-chamber geometry and equivalence ratio combination. Note that while ΔP was much greater for PC 1 than for PC 2, jet momentum flux for each PC was similar for an igniter-equivalence ratio combination. The reason is that jet momentum flux is directly proportional to ΔP and nozzle area, A_T. The radial nozzles for PC 2 had a 50% larger diameter than PC 1 (i.e., 1.2 mm vs. 0.8 mm), and hence a nozzle hole area that was 2.25 times greater, which is comparable to the difference in ΔP for PC 1 relative to PC 2.

Gas temperature is presented in Figure 8 (a) and 8 (b) for PC 1 and PC 2, respectively. Peak temperatures only varied for changes in equivalence ratio due to the lower amount fuel energy for leaner conditions. There were variations, however, in the temperature profile for the two pre-chamber tips evaluated. Relative to PC 2, PC 1 featured a more rapid increase in temperature followed by a plateau near the peak temperature (~25°). Conversely, PC 2 had a steeper temperature decline shortly after reaching the peak value, with little to no high-temperature plateau region. The slower increase in temperature and more rapid decline past the peak for PC 2 mostly is the result of the larger hole area that is less effective in producing and maintaining pressure build-up along with the smaller internal volume that results in a greater fraction of thermal energy being lost to heat transfer.

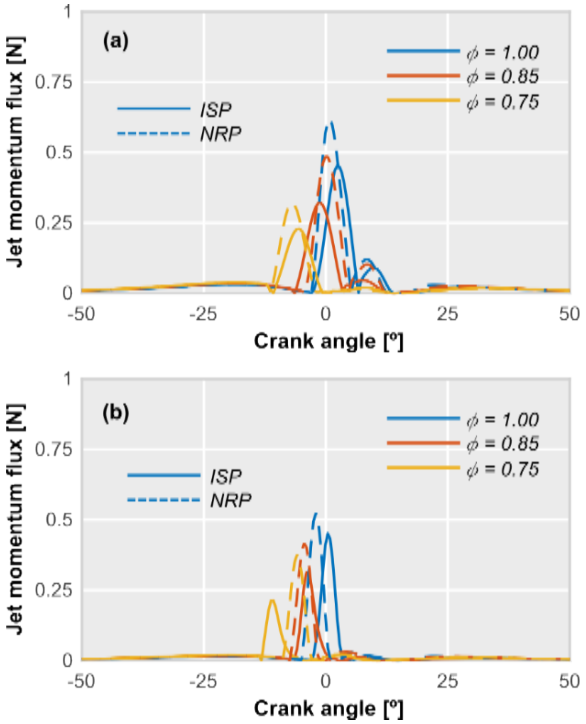

Figure 7. Radial jet momentum flux profiles for the three operating points of PC 1 (a) and PC 2 (b) and both ignition systems. The solid line corresponds to the ISP system, the dashed line corresponds to the NRP system. The blue, orange and yellow lines correspond to ϕ = 1.00, ϕ = 0.85 and ϕ = 0.75, respectively.

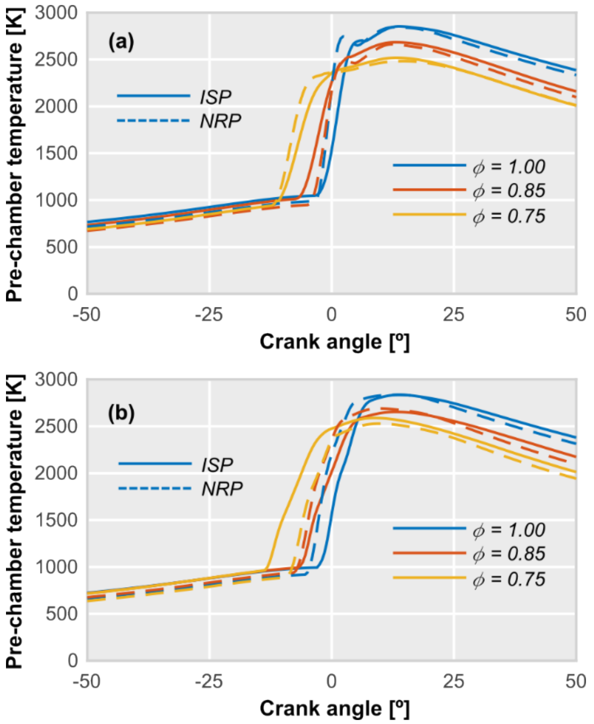

Figure 8. Pre-chamber temperature profiles for the three operating points of PC 1 (a) and PC 2 (b) and both ignition systems. The solid line corresponds to the ISP system, the dashed line corresponds to the NRP system. The blue, orange and yellow lines correspond to ϕ = 1.00, ϕ = 0.85 and ϕ = 0.75, respectively.

Jet velocity estimation

Jet penetration length and velocity were estimated using the 1D jet model, with the jet momentum flux and mass flow rate calculated by the 1D wave action model that used AHRR from the experimental measurements. In Figures 9 (a) and 9 (b), the time evolution of the jet penetration length is plotted for both ignition systems and pre-chamber tips. To normalize the different ejection timings from the different pre-chamber geometries and equivalence ratio cases, a so-called 'Start of Ejection' (SoE) is defined as the crank angle position where pressure difference between pre-chamber and main chamber (ΔP) is 0.5 bar. The SoE allows phase differences due to different ignition timings to be accounted for. The methodology is the same as was used in previous work [21]. In the mentioned Figure, the zero intercept of the abscissa is defined as crank angle after start of ejection (ASoE). The rate of jet penetration is directly proportional to the jet momentum flux, with higher momentum flux values resulting in faster penetration. Accordingly, slower jet penetration is predicted at the mixtures become increasingly lean. It is also evident that for a given equivalence ratio that faster jet penetration was produced with NRP ignition relative to ISP ignition. The increase in the rate of penetration with NRP ignition was greatest with PC 1, whereas there was virtually no change in jet penetration rate with NRP or ISP ignition for PC 2.

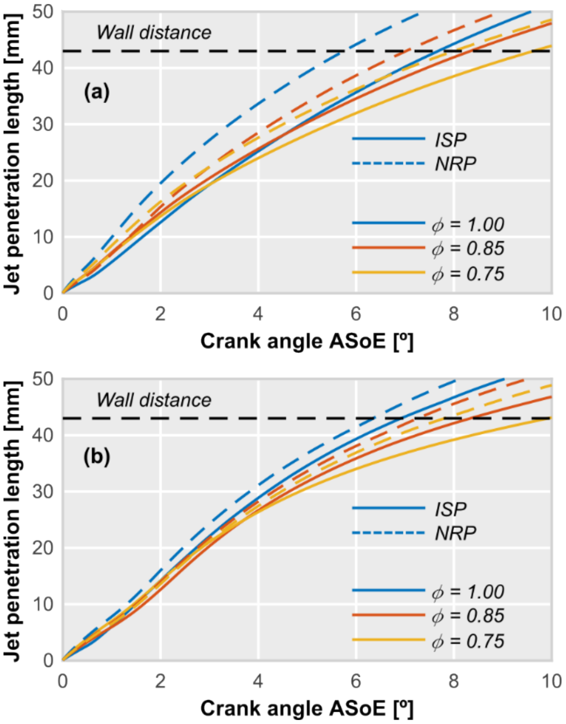

Figure 9. Jet penetration length profiles for the three operating points of PC 1 (a) and PC 2 (b) and both ignition systems. The solid line corresponds to the ISP system, dashed line corresponds to the NRP system. The blue, orange and yellow lines correspond to ϕ = 1.00, ϕ = 0.85 and ϕ = 0.75, respectively. Black dashed line represents the distance to the bore limit.

Numerical comparison between heat release rates and jet performance predictions

Model predicted values of jet momentum flux and penetration rate that make use of simulated AHRR via a Wiebe function with tuned CA50 instead of measured AHRR as a boundary condition for the 1D wave action model is discussed in here. In Figure 10, pre-chamber AHRR profiles from the experiment and 2 simulation methodologies are compared for PC 1 at the stoichiometric condition and using the NRP igniter. Similar results were observed for all other operating points. Simulation predicted AHRR (yellow) came from suitable hypotheses from literature and previous knowledge prior to obtain experimental results. Simulation matching experimental AHRR (orange) was carried out after obtaining experimental results, which its aim was to simulate a comparable AHRR to the experimental one. For this study, the peak AHRR value was selected to be matched because it drives the peak of the jet momentum flux and thus, the maximum jet penetration length. The start of combustion and combustion duration were relatively well matched, which meant the profile width and hence the combustion duration was likewise similar to the experiment. There was a slight delay in combustion initiation for the predicted AHRR simulation, which in turn delayed pre-chamber pressurization. Note that complex geometric effects of the pre-chamber could not be integrated into a 1D model, which also likely contributed to the mismatch of AHRR evolution between the experiment and both simulation methods.

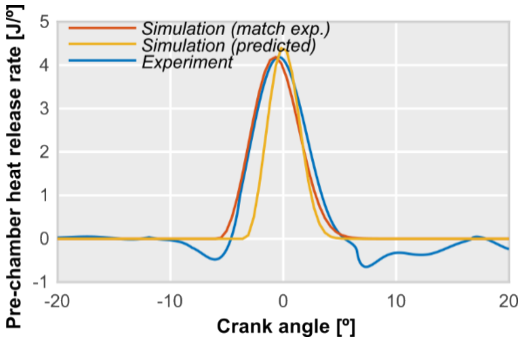

Figure 10. Experimental and simulated apparent heat release rates for stoichiometric point operating with PC 1 and NRP system. The blue line corresponds to the experimental measured profile, the orange line corresponds to the simulated profile matching the experiment and the yellow line corresponds to the simulated profile coming from a predicted combustion process.

Pre- and main-chamber ΔP evolution from the experiment and the two simulation cases is plotted in Figure 11 for PC 1 at the stoichiometric condition and using the NRP igniter. Since ΔP is highly dependent on AHRR as already discussed, it is no surprise that ΔP trends in Figure 11 closely track with AHRR trends in Figure 10. Nonetheless, the peak simulated pressures and total profile durations were noticeably lower for both simulation methodologies – particularly the method that used a predicted pre-chamber AHRR profile. For the simulation methodology that made use of the experimentally matched pre-chamber AHRR, the differences are likely related to insufficient capture of geometric effects relative to the real case. For the simulation methodology that used predicted PC heat release, the difference is mostly attributed to an underprediction of overall heat release duration and total heat release.

As explained previously, pre-chamber pressurization significantly impacts the jet momentum flux with larger ΔP promoting more complete penetration into the main chamber before ignition is initiated. Thus, the jet momentum flux profile potted in Figure 12 for the simulation that used predicted PC heat release had a corresponding reduction and duration. Moreover, the start of the jet ejection process was delayed by approximately 2 crank angles.

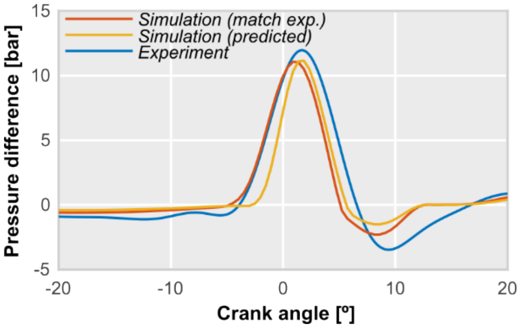

Figure 11. Experimental and simulated pressure difference traces for stoichiometric point operating with PC 1 and NRP system. The blue line corresponds to the experimental measured profile, the orange line corresponds to the simulated profile matching the experiment and the yellow line corresponds to the simulated profile coming from a predicted combustion process.

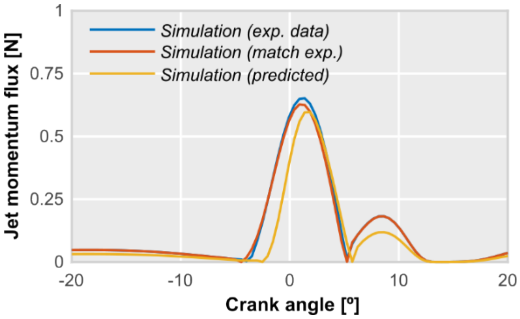

Figure 12. Simulated jet momentum flux profile for stoichiometric point operating with PC 1 and NRP system. The blue line corresponds to the numerical results coming directly from the experimental data, the orange line corresponds to the simulated profile matching the experiment and the yellow line corresponds to the simulated profile coming from a predicted combustion process.

A comparison of the jet penetration length between the simulations with the different modeling methodologies and the simulation using experimental AHRR is plotted in Figure 13 for the PC 1 at the stoichiometric condition and with the NRP igniter. The rate of predicted jet penetration into the main combustion chamber is impacted by the modeling method selected, with the experimental pre-chamber heat release predicting the fastest penetration and the simulation predicted pre-chamber heat release that uses the Wiebe function predicting the slowest. There is roughly a 0.5 crank angle spread in the prediction when the jet would impinge on the 43 mm radius cylinder bore. It is interesting to note that the differences manifest themselves within the first 1 crank angle degree after the start of ejection, with little change thereafter.

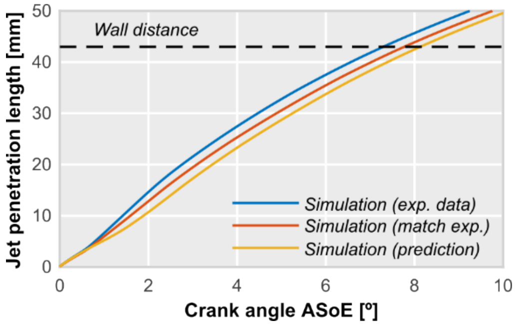

Figure 13. Simulated jet penetration length profile for stoichiometric point with PC 1 and NRP system. The blue line corresponds to the numerical results coming directly from the experimental data, the orange line corresponds to the simulated profile matching the experiment and the yellow line corresponds to the simulated profile coming from a predicted combustion process.

As stated in the Experimental Procedure section, the experimental calculation of the jet velocity of radial nozzles was only possible for PC 2, since the axial nozzle of PC 1 prevents the proper visualization of radial jets. Furthermore, jet luminosity was much weaker for the leanest equivalence ratio case, which made it difficult to properly distinguish the jet head. Accordingly, only jet velocity for ϕ=0.85 and ϕ=1.0 are shown in Figure 14 for PC 2 utilizing the NRP ignition system. Simulated jet velocities were obtained utilizing the slope of the jet penetration length at the first 0.1 ms of the jet ejection process (where experimental data were available). Jet-exit velocity was slowest for predictions that made use of the predicted AHRR model inputs by roughly 10%. Jet-exit velocity predictions that used simulation data based on measured AHRR, however, were much closer to the experimentally measured values.

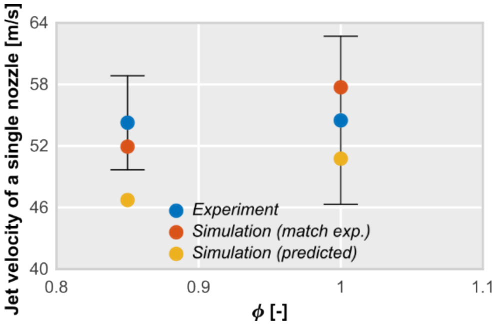

Figure 14. Experiment, simulation matching the experiment and simulation with predicted combustion process jet velocity estimation for PC 2 and NRP system. The blue dot corresponds to the experimental results, the orange dot corresponds to the simulation matching the experiment and the yellow dot corresponds to the simulation coming from a predicted combustion process. The error bars represent one standard deviation of experimental data.

Conclusions

Two different pre-chamber tips were experimentally tested using two different ignition systems in a 4-stroke, optically-accessible SCRE; with experiments focused on the relationship between slow and fast burn ignition systems, equivalence ratio and pre-chamber design. Two different 1D simulation methodologies were used to numerically evaluate pre-chamber performance in terms of jet momentum flux, pre-chamber temperature, jet penetration and jet-exit velocity. A 1D wave action software with two different models, one with the experimental heat release rate within the pre-chamber and the other with the simulated heat release rate within the pre-chamber were evaluated. Experimental AHRR inside the pre-chamber was computed from the pressure trace recorded by a dedicated pressure transducer and was also estimated for 1D wave action simulation using a Wiebe function with combustion phasing tuned to the experiment value. The main conclusions of this work are as follows:

- PC 1 exhibited a steeper initial slope and a greater maximum peak of the AHRR profile compared to PC 2 regardless of the igniter used to ignite the pre-chamber mixture. The NRP system featured a steeper initial slope and a greater peak heat release rate compared with ISP system for both pre-chamber geometries.
- Pre-chamber pressurization and jet momentum flux through the nozzles were found to be dependent both on the combustion duration and pre-chamber geometry. Shorter combustion duration tended to increase the difference in pressure between chambers, increasing the jet momentum and the ability of the jets to sweep

the main chamber. Moreover, the smaller total pre-chamber nozzle hole area for PC 1 was found to hinder jet ejection.

- The numerical model simulations produced similar AHRR profile results relative to the experiments. The simulation that made use of the measured pre-chamber AHRR produced the best match with experimental, while the Wiebe function approach to predicting pre-chamber heat release produced AHRR with delayed phasing of up to 3 crank angles and a much shorter combustion duration.
- The lower estimation in total pre-chamber heat release for the simulation that used predicted pre-chamber AHRR led to an associated underprediction in pressure difference between the pre- and main-chambers, jet momentum flux, rate of jet penetration, and jet-exit velocity. The reasons for the differences are unclear~~,~~ but are likely related to poor capture of geometry effects within the pre-chamber such as wall heat transfer and nozzle quenching phenomena. These results highlight the need for a more robust pre-chamber combustion prediction methodology.

References

1. Ayala, F. A. and Heywood, J. B., "Lean SI Engines: The role of combustion variability in defining lean limits", 8th International conference on Engines for Automobiles, 2007, doi:10.4271/2007-24-0030.
2. Ayala, F. A., Gerty, M. D., and Heywood, J. B., "Effects of combustion phasing, relative air-fuel ratio, compression ratio, and load on SI engine efficiency." SAE Transactions (2006): 177-195, doi:10.4271/2006-01-0229.
3. Attard, W. P., Bassett, M., Parsons, P., and Blaxill, H., "A new combustion system achieving high drive cycle fuel economy improvements in a modern vehicle powertrain", SAE Technical Paper 2011-01-0664, 2011, doi:10.4271/2011-01-0664.
4. Attard, W. P., and Parsons, P., "A normally aspirated spark initiated combustion system capable of high load, high efficiency and near zero NOx emissions in a modern vehicle powertrain", *SAE Int. J. Engines* 3(2):269-287, 2010, doi:10.4271/2010-01-2196.
5. Attard, W. P., and Blaxill, H., "A lean burn gasoline fueled pre-chamber jet ignition combustion system achieving high efficiency and low NOx at part load", SAE Technical Paper 2012-01-1146, 2012, doi:10.4271/2012-01-1146.
6. Biswas, S., and Qiao, L., "Ignition of ultra-lean premixed H2/air using multiple hot turbulent jets generated by pre-chamber combustion", Applied Thermal Engineering, 132, 102-114, 2018, doi:10.1016/j.applthermaleng.2017.11.073.
7. Mastorakos, E., Allison, P., Giusti, A., De Oliveira, P., et al. "Fundamental aspects of jet ignition for natural gas engines", *SAE Int. J. Engines* 10(5):2429-2438, 2017, doi:10.4271/2017-24-0097.
8. Allison, P. M., De Oliveira, M., Giusti, A., and Mastorakos, E., "Pre-chamber ignition mechanism: Experiments and simulations on turbulent jet flame structure", Fuel, 230, 274-281, 2018, doi:10.1016/j.fuel.2018.05.005.
9. Bunce, M., Blaxill, H., Kulatilaka, W., and Jiang, N. "The effects of turbulent jet characteristics on engine performance using a pre-chamber combustor", SAE Technical Paper 2014-01-1195, 2014, doi:10.4271/2014-01-1195.
10. Muller, M., Freeman, C., Zhao, P., and Ge, H. "Numerical simulation of ignition mechanism in the main chamber of turbulent jet ignition system", *Internal Combustion Engine Division Fall Technical Conference* (Vol. 51999, p. V002T06A010). American Society of Mechanical Engineers, doi:10.1115/ICEF2018-9587.
11. Gentz, G., Gholamisheeri, M., and Toulson, E. "A study of a turbulent jet ignition system fueled with iso-octane: Pressure trace analysis and combustion visualization", Applied Energy, 189, 385-394, 2017, doi:10.1016/j.apenergy.2016.12.055.
12. Gholamisheeri, M., Wichman, I. S., and Toulson, E. "A study of the turbulent jet flow field in a methane fueled turbulent jet ignition (TJI) system", Combustion and Flame, 183, 194-206, 2017, doi:10.1016/j.combustflame.2017.05.008.
13. Jamrozik, A., Tutak, W., Kociszewski, A., and Sosnowski, M. "Numerical simulation of two-stage combustion in SI engine with prechamber", Applied Mathematical Modelling, 37(5), 2961-2982, 2013, doi:10.1016/j.apm.2012.07.040.
14. Thelen, B. C., and Toulson, E., "A computational study of the effects of spark location on the performance of a turbulent jet ignition system" SAE Technical Paper 2016-01-0608, 2016, doi:10.4271/2016-01-0608.
15. Wang, N., Liu, J., Chang, W. L., and Lee, C. F., "A numerical study of the combustion and jet characteristics of a hydrogen fueled turbulent hot-jet ignition (THJI) chamber", *International journal of hydrogen energy*, 43(45), 21102-21113, 2018, doi:10.1016/j.ijhydene.2018.09.156.
16. Novella, R., Pastor, J., Gomez-Soriano, J., and Barbery, I., et al., "Experimental and numerical analysis of passive pre-chamber ignition with EGR and air dilution for future generation passenger car engines" SAE Technical Paper 2020-01-0238, 2020, doi:10.4271/2020-01-0238.
17. Benajes, J., Novella, R., Gómez-Soriano, J. and Barbery, I. et al. "Computational assessment towards understanding the energy conversion and combustion process of lean mixtures in passive pre-chamber ignited engines", Applied Thermal Engineering, 178, 115501, 2020, doi:10.1016/j.applthermaleng.2020.115501.
18. Jamrozik, A, "Lean combustion by a pre-chamber charge stratification in a stationary spark ignited engine", *Journal of Mechanical Science and Technology*, 29(5), 2269-2278, 2015, doi:10.1007/s12206-015-0145-7.
19. Heyne, S., Meier, M., Imbert, B., and Favrat, D., "Experimental investigation of prechamber autoignition in a natural gas engine for cogeneration", Fuel, 88(3), 547-552, 2019, doi:10.1016/j.fuel.2008.09.032.
20. Korb, B., Kuppa, K., Nguyen, H. D., and Dinkelacker, F., et al. "Experimental and numerical investigations of charge motion and combustion in lean-burn natural gas engines", Combustion and Flame, 212, 309-322, 2020, doi:10.1016/j.combustflame.2019.11.005.
21. García-Oliver, J. M., Niki, Y., Rajasegar, R. and Novella, R., et al. "An experimental and one-dimensional modeling analysis of turbulent gas ejection in pre-chamber engines", Fuel, 299, 120861, 2021, doi: 10.1016/j.fuel.2021.120861.
22. Novella, R., Gomez-Soriano, J., Martinez-Hernandiz, P. J. and Libert, C. et al. "Improving the performance of the passive pre-chamber ignition concept for spark-ignition engines fueled with natural gas", Fuel, 290, 119971, 2021, doi:10.1016/j.fuel.2020.119971.
23. Benajes, J., Novella, R., Gómez-Soriano, J. and Martinez-Hernandiz, P. J. et al. "Evaluation of the passive pre-chamber ignition concept for future high compression ratio turbocharged spark-ignition engines", Applied Energy, 248, 576-588, 2019, doi:10.1016/j.apenergy.2019.04.131.
24. López, J. J., Novella, R., Gomez-Soriano, J. and Martinez-Hernandiz, P. J. et al., "Advantages of the unscavenged pre-chamber ignition system in turbocharged natural gas engines for automotive applications", Energy, 218, 119466, 2021, doi:10.1016/j.energy.2020.119466.

25. Biswas, S. and Ekoto, I., "Detailed Investigation into the Effect of Ozone Addition on Spark Assisted Compression Ignition Engine Performance and Emissions Characteristics" SAE Technical Paper 2019-01-0966, 2019, doi:10.4271/2019-01-0966.
26. Biswas, S., Ekoto, I., Singleton, D. and Mixell, K. “Nanosecond Pulsed Ignition for Automotive Applications: Performance and Emissions Characteristics of Gasoline Combustion in an Optical Engine”, SAE Technical Paper, 2021-01-0475, 2021, doi:10.4271/2021-01-0475.
27. Pastor, J. V., López, J. J., García, J. M., and Pastor, J. M., “A 1D model for the description of mixing-controlled inert diesel sprays”, Fuel, 87(13-14), 2871-2885, 2008, doi:10.1016/j.fuel.2008.04.017.
28. Desantes, J. M., Pastor, J. V., García-Oliver, J. M., and Pastor, J. M. “A 1D model for the description of mixing-controlled reacting diesel sprays”, Combustion and Flame, 156(1), 234-249, 2009, doi:10.1016/j.combustflame.2008.10.008.
29. Desantes, J. M., García-Oliver, J. M., Xuan, T., and Vera-Tudela, W. “A study on tip penetration velocity and radial expansion of reacting diesel sprays with different fuels”, Fuel, 207, 323-335, 2017, doi:10.1016/j.fuel.2017.06.108.
30. Chang, J., Güralp, O., Filipi, Z., and Assanis, D. et al., "New Heat Transfer Correlation for an HCCI Engine Derived from Measurements of Instantaneous Surface Heat Flux", SAE Technical Paper 2004-01-2996, 2004, doi:10.4271/2004-01-2996.
31. Duong, J., Wellander, R., Hyvönen, J. and Andersson, Ö. et al. “High Speed Combustion Imaging in a Large Bore Gas Engine: The Relationship Between Pre-and Main Chamber Heat Release” *ASME International Mechanical Engineering Congress and Exposition* (Vol. 56345, p. V08AT09A022). American Society of Mechanical Engineers, doi:10.1115/IMECE2013-64286.
32. Heywood, J. B., “Internal combustion engine fundamentals” McGraw-Hill Education, 2018.
33. Hlaing, P., Echeverri Marquez, M., Shankar, V., and Cenker, E., et al. “A study of lean burn pre-chamber concept in a heavy duty engine”, SAE Technical Paper 2019-24-0107, 2019, doi:10.4271/2019-24-0107.

Contact Information

Pablo Jose Martinez Hernandiz. Ph.D Student. CMT-Motores Térmicos. Universitat Politècnica de València (UPV). Valencia, Spain. pabmarh2@mot.upv.es

Acknowledgments

P. J. Martinez-Hernandiz is partially supported by an FPI contract (FPI-S2-19-21993) of the “Programa de Apoyo para la Investigación y Desarrollo (PAID-05-19)” of the Universitat Politècnica de València. The authors would like to thank Alberto Garcia for his dedicated support of the Gasoline Combustion Fundamentals Laboratory. Part of this work was performed at the Combustion Research Facility, Sandia National Laboratories, Livermore, CA. Financial support was provided by the U.S. Department of Energy, Vehicle Technologies Office. Sandia National Laboratories is a multi-mission laboratory managed and operated by National Technology and Engineering Solutions of Sandia, LLC., a wholly-owned subsidiary of Honeywell International, Inc., for the U.S. Department of Energy’s National Nuclear Security Administration under contract DE-NA0003525.

Definitions/Abbreviations

AHRR	Apparent heat release rate [J/°]
ASoE	After start of ejection
At	Total nozzle area
CA	Crank angle [°]
CFD	Computational fluid dynamics
CO	Carbon monoxide
CoV	Covariance
Cp	Specific heat capacity at constant pressure
EVO	Exhaust valve opening
HC	Hydrocarbon
HRR	Heat release rate [J/°]
IMEPg	Intake manifold effective pressure (gross) [bar]
ISP	Inductive spark plug.
IVC	Intake valve closing
NOx	Nitrogen oxides
NRP	Nanosecond repetitive pulse
OH*	Hydroxyl radical.
RCM	Rapid compression machine
RPM	Revolutions per minute
SoE	Start of ejection
ST	Spark timing
TDC	Top dead center
TJI	Turbulent Jet Ignition
γ	Specific heat ratio
ΔP	Pressure difference between pre-chamber and main chamber [bar]
ϕ	Equivalence ratio